Thermal Management Key Performance Parameter Development and System Analysis for the SUSAN Electrofan Aircraft

Erik J. Stalcup[1], Timothy P. Dever[2], and Jonah J. Sachs-Wetstone[3]
NASA Glenn Research Center, Cleveland, Ohio 44135, U.S.A.

A set of key performance parameters (KPPs) for thermal management system (TMS) components was developed for use in system sizing and analysis. These KPPs were defined at three different levels of performance corresponding to different ranges of Technology Readiness Levels. KPP values were determined based on a large dataset that includes analysis and testing data from literature, NASA-funded research, and commercial product datasheets. These KPPs were then used to perform a TMS sizing and analysis of the SUbsonic Single Aft eNgine (SUSAN) aircraft. Total TMS mass, power consumption, and drag is quantified at each KPP level, showing decreasing trends as the level of technology improves.

I. Nomenclature

G	=	thermal conductance
$\dot{m}$	=	coolant mass flow rate
P	=	power
Q	=	component heat load
$T_{hotspot}$	=	component hotspot temperature
T_{in}	=	component inlet coolant temperature
T_{out}	=	component outlet coolant temperature
$\dot{V}$	=	coolant volumetric flow rate
Δp	=	coolant pressure drop
$\varepsilon_{cooling}$	=	cooling effectiveness
ε_{HX}	=	heat exchanger effectiveness

II. Introduction

Electrified aircraft thermal management system (TMS) design has been a subject of recent interest with several different architectures and thermal management technologies under consideration [1–3]. These aircraft produce most or all their propulsive power using electrical powertrains, so they generate orders of magnitude more waste heat than electrical power systems on traditional fuel-burning aircraft. Furthermore, the heat is more difficult to reject than compared to the combustion process for jet engine propulsion, wherein most of the heat is discharged through the exhaust gas. For electrified propulsion, the heat is typically generated by electrical losses in motor windings, power electronic devices, battery cells, and other components that are not as intrinsically coupled to the freestream air as a turbine engine. Therefore, it is a significant challenge to design a TMS that can reject this heat without negating the benefits of electrification through additional TMS weight, drag, and power consumption. Many previous studies have sized and modeled electrified aircraft TMSs, but few have given consideration to the failure modes of the system and the required redundancy of components. Furthermore, many studies do not size the TMS or evaluate performance in the full range of environments in which current aircraft are certified to fly. This study aims to quantify the weight,

[1] Aerospace Engineer, Thermal Systems and Transport Processes Branch, non-AIAA member.
[2] Electrical Engineer, Diagnostics and Electromagnetics Branch, AIAA member.
[3] Control Systems Engineer, Intelligent Control and Autonomy Branch, AIAA member.

drag, and power consumption of a realistically sized and redundant TMS architecture using the SUbsonic Single Aft eNgine (SUSAN) aircraft concept.

SUSAN is a 180-passenger regional aircraft concept designed by National Aeronautics and Space Administration (NASA) with the intent of reducing emissions within the 2035–2040 time frame through several advanced aircraft technologies made possible in large part by Electrified Aircraft Propulsion (EAP) [4]. Although the SUSAN aircraft is the size of a large single-aisle aircraft, it is categorized as a regional jet since its range is comparable to current regional jets. The current design features a traditional tube and wing design with a single aft turbofan that produces 35% of the total aircraft thrust. Additional mechanical shaft power is also harnessed from the turbofan and converted to electric power via an array of generators to drive wing-mounted electric propulsors that produce the remaining 65% of aircraft thrust. Supplemental power from rechargeable batteries allows for optimization of the performance and sizing of the turbofan. Power from a single-use battery is available in the event of a power loss from the engine to power the propulsion system and would allow for safe landing of the aircraft. The design flight profile for SUSAN is typical for regional jets, with a design range of 2,500 nmi, an economic range of 750 nmi, at Mach 0.775, and an initial cruise altitude of 35,000 ft [5].

The following sections describe the key performance parameter (KPP) approach to sizing a TMS at varying levels of technology. Definitions and data sources for the KPP values are detailed. Then the SUSAN TMS design is described, followed by a sizing study and analytical modeling. Concurrent publications utilize this same methodology for a preliminary TMS sizing of the SUSAN aircraft and a sizing of large hybrid-electric turboprop.

III. Key Performance Parameters

A primary objective of the design and sizing of the SUSAN TMS was to quantify the impact of a realistically sized and redundant TMS architecture on the overall airplane performance. The impacts include the weight, power draw, and drag that the TMS contributes to the system. Another objective was to quantify these impacts at three different levels of TMS component performance corresponding to different ranges of technology development. Evaluation at these three levels illustrates the change in TMS impact as technology progresses from the current state of the art to future levels. To this end, a set of key performance parameters (KPPs) was developed to define the thermal performance, fluid performance, power consumption, and weight of each component in the SUSAN TMS. The KPPs relevant to each type of TMS component is discussed in the following sections. This KPP approach was also taken for the SUSAN Electrical Power System (EPS) components and is detailed in prior publications [5,6].

The levels are based on NASA's Technology Readiness Level (TRL) scale and are summarized in Table 1. To assign values to each KPP at each TRL range, data from several sources were compiled to provide a broad assessment of current and future TMS component performance. When compiling this data, focus was given to component designs that are specific to aeronautical applications. In some cases, data was not available in the given TRL range for aeronautical applications, so other sources were considered from similar automotive or space applications. For example, at present there is little public data available on TRL 5+ liquid-cooled battery designs for aviation, so the KPP values are based on data for liquid-cooled automotive batteries for electric and hybrid-electric cars. Additionally, focus is given to full component designs, rather than subcomponents or parts. For example, KPP values for liquid-cooled converters are based on converter designs, rather than individual transistor or transistor module cooling solutions.

For the TRL 5+ KPP level, representing the state of the art, sources include commercial off-the-shelf (COTS) product datasheets, specifications, and manuals; published and NASA-internal test data for COTS products; and other published data and analysis of TRL 5+ technologies from journal articles, conference papers, whitepapers, etc. For the TRL 3-4 KPP level, which represents current research, sources include test data and analysis from NASA internal technology development; test data and analysis from NASA-funded technology development, including multiple Small Business Innovation Research (SBIR) programs and projects funded under the Aeronautics Research Mission Directorate (ARMD); and other published data and analysis of TRL 3-4 technologies. For the TRL 1-2 KPP level, values are projections of future technology development based on the other two KPP levels.

Table 1 Key Performance Parameter Levels

KPP Level	KPP Level Description	Sources for KPP Values
TRL 5+	State of the art	• Commercial product datasheets • Commercial product test data • Other published test data or analysis of TRL 5+ technologies
TRL 3-4	Current research	• Testing and analysis from NASA internal technology development • Testing and analysis from NASA-funded technology development • Other published test data or analysis of TRL 3-4 technologies
TRL 1-2	Future projections	• Projections based on higher TRL level data and analysis • Published analysis of TRL 1-2 technologies

Since the SUSAN TMS utilizes single-phase liquid cooling, the KPPs presented here are specific to single-phase liquid cooling solutions. However, a similar approach can be taken for air-cooled, two-phase, or other solutions. KPPs are defined and values are assigned within the following categories: heat acquisition, heat transport, and heat rejection. Heat acquisition KPPs characterize the thermal and fluid performance of cooling of motors/generators, converters, battery modules, and circuit interrupters. Heat transport KPPs characterize the power draw and weight of fluid pumps and heat pumps. Heat rejection KPPs characterize the thermal and fluid performance and weight of ram-air heat exchangers. These KPPs are defined so that they represent the minimum number of parameters needed to characterize the weight, power draw, and drag of the TMS. They are also defined so that they can be directly utilized for high-level thermal/fluid modeling and analysis. It is possible that multiple KPPs could be combined to provide a single coefficient of performance (COP) that represents, for example, a combined thermal/fluid performance. This is a useful metric for comparing overall performance among different designs. However, it is not convenient as a direct modeling input where values such as conductance and pressure drop are needed separately. The definition of each of these KPPs and the selection of their values are described as follows.

A. Heat Acquisition

For the SUSAN aircraft, heat acquisition is concerned with how heat is collected from the heat producing components which include the motors/generators, converters, battery modules, and circuit interrupters. The heat load and the weight of the overall component is characterized by the efficiency and specific power KPPs, which are described in a prior publication [6]. As previously stated, this study only focuses on single-phase liquid cooling. Both indirect and direct liquid cooling are considered. In this context, indirect cooling generally refers to cold plate technologies, and direct cooling refers to immersion cooling.

The thermal performance KPP should describe how effective a given cooling solution is at removing heat relative to the maximum possible heat that can be removed by the coolant. From the energy equation

$$Q = \dot{m} c_p (T_{out} - T_{in}) \tag{1}$$

where Q is the heat load from the component, $\dot{m}$ is the coolant mass flow rate, c_p is the isobaric specific heat of the coolant, T_{out} is the outlet coolant temperature, and T_{in} is the inlet coolant temperature. The maximum possible rejection occurs when the coolant outlet temperature is equal to the component hotspot temperature:

$$Q_{max} = \dot{m} c_p \left(T_{hotspot} - T_{in}\right) \tag{2}$$

Analogous with the definition of heat exchanger effectiveness [7], a cooling effectiveness is used for the thermal performance KPP and is defined as

$$\varepsilon_{cooling} = \frac{Q}{Q_{max}} = \frac{Q}{\dot{m} c_p \left(T_{hotspot} - T_{in}\right)} = \frac{T_{out} - T_{in}}{T_{hotspot} - T_{in}} \tag{3}$$

In steady-state conditions, $\varepsilon_{cooling}$ will always be between 0 and 1. This can also be written in terms of a thermal conductance G between the hotspot of the component and the fluid:

$$\varepsilon_{cooling} = \frac{Q}{\dot{m}c_p\left(T_{hotspot} - T_{in}\right)} = \frac{\left(\frac{Q}{\Delta T}\right)}{\dot{m}c_p} = \frac{G}{\dot{m}c_p} \tag{4}$$

In this interpretation, the thermal conductance has been normalized by the coolant flow rate. This removes sensitivity to the power level of the component and allows for a fair comparison between designs, assuming that the coolant flow rate must increase linearly with the heat load to produce the same temperature change when scaling up a given design. This is the case when power is scaled up and heat fluxes remain the same, such as when adding more parallel slot cooling passages for a larger stator running the same current. However, this may not be the case when power is scaled up and heat fluxes also increase, such as when increasing flow through cooling passages for the same sized stator running a higher current. In this situation, the relationship between the heat dissipation and the coolant flow rate may not be linear and is described by the heat transfer coefficient or Nusselt number. However, these relationships can often be approximated as linear if the design is not scaled too far from the original operating point.

The fluid performance KPP should also scale with the component power level. The natural parameter is the ratio of heat load to pumping power:

$$\frac{Q}{P} = \frac{Q}{\Delta p \dot{V}} \tag{5}$$

where P is the pumping power, Δp is the coolant pressure drop across the component, and $\dot{V}$ is the coolant volumetric flow rate.

$\varepsilon_{cooling}$ and Q/P were both calculated for all the designs in the compiled dataset. Since these two KPPs are often competing factors, it is useful to plot both values to assess the level of performance for all designs across the three TRL ranges. In the following sections, plots are presented with regions spanning a range of KPP values. Each region encompasses the KPPs calculated for the designs in each TRL range. The optimal selection of KPP values for a particular TMS design will depend on the architecture and mission profile, but the highest performing designs lie toward the upper right of these regions. The KPP values chosen for the SUSAN TMS design and analysis are indicated by a star (★) in each plot.

The KPP plots for motors/generators, converters, and battery modules are shown in Figs. 1 through 3. The sources of data are summarized in Tables 2 through 4. For motors/generators and converters, the KPPs are based on continuous power operation. For battery modules, some data is based on steady-state operation, but most sources are concerned with thermal performance during transient charging/discharging. For such cases, the KPPs are calculated using Eq. (4) with $T_{hotspot}$ taken at peak values, typically at the end of the transient, and Q approximated as an average heat load over the whole transient using the value at 50% state of charge.

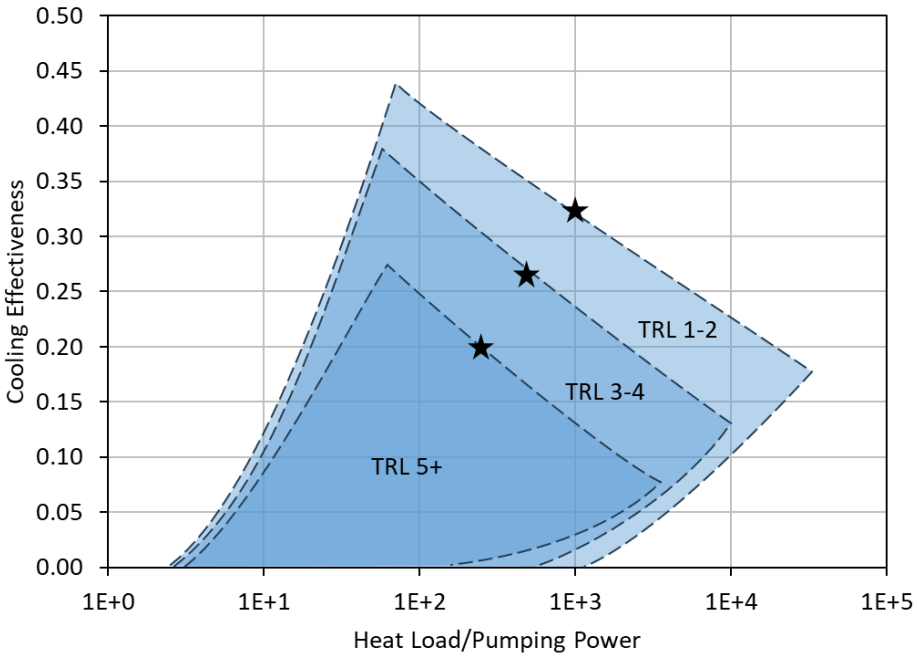

Fig. 1 Electric motor and generator KPPs

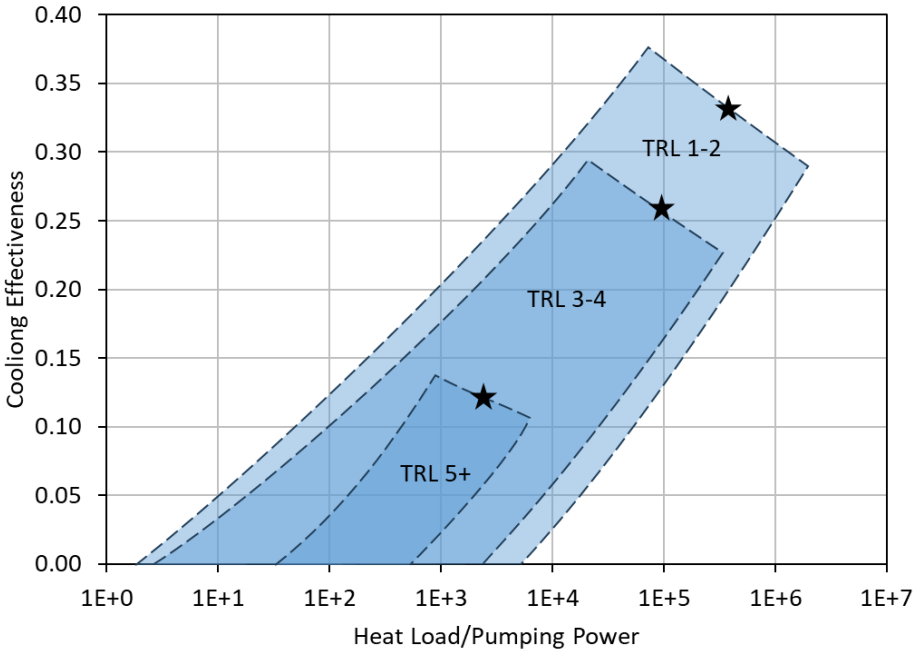

Fig. 2 Converter KPPs

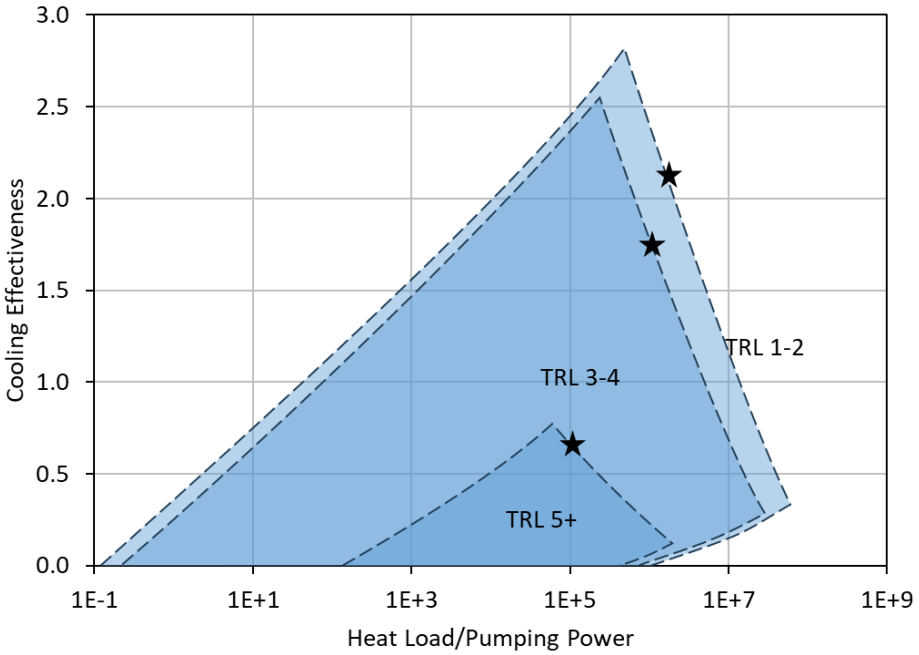

Fig. 3 Battery module KPPs

Table 2 Electric Motor and Generator Cooling Designs

Description	Cooling Method	Coolant	Source
Cooling channels embedded in winding supports	Indirect	Water/Glycol	[8]
Water jacket cooling for motor and inverter	Indirect	Water	[9]
Cooling channels embedded in stator core	Indirect	Water/Glycol	[10]
Water cooled casing with heat extraction fins	Indirect	Water/Glycol	[11]
Various designs	Indirect	Water/Glycol	Datasheets and test data of 17 different commercial aerospace and automotive motors
Various designs	Indirect	Various	NASA funded and internal projects
Immersion-cooled stator windings	Direct	PAO	[12]
Coolant conduits embedded in windings	Direct	PAO Water	[13]
Immersion-cooled stator windings	Direct	Water/Glycol	[14]

Table 3 Converter Cooling Designs

Description	Cooling Method	Coolant	Source
Traditional cold plate	Indirect	Water/Glycol	[15]
Traditional cold plate and heat spreader	Indirect	Water/Glycol	[16]
Jet impingement on finned baseplate	Indirect	Water/Glycol	[17]
Liquid metal cold plate	Indirect	Gallium alloy	[18,19]
Dual-sided cooling with additively manufactured cold plate	Indirect	Water	[20]
Integrated liquid-cooled baseplate	Indirect	Water	[21]
Dual side cooling	Indirect	Water	[22]
Baseplate cooling Jet impingement on finned baseplate	Indirect Direct	Water/Glycol Oil, PAO	[23,24]
Various designs	Indirect	Water/Glycol	Datasheets and test data of 6 different commercial automotive converters
Various designs	Indirect	Various	NASA funded and internal projects
Immersion cooling	Direct	Oil	[25]

Table 4 Battery Module Cooling Designs

Description	Form Factor	Cooling Method	Coolant	Source
Cooling channel structures inserted into gaps between cells	Cylindrical	Indirect	Water	[26]
Distributed water-cooling jackets	Cylindrical	Indirect	Water	[27]
Mini-channel cooling structure	Cylindrical	Indirect	Water	[28]
Serpentine cooling passages between cells	Cylindrical	Indirect	Water	[29]
Various designs	Cylindrical Prismatic	Indirect	Various	NASA funded and internal projects
Microchannel cold plates between cells	Prismatic	Indirect	Water	[30]
Traditional cold plate Immersion cooling	Cylindrical	Indirect Direct	Water/Glycol Hydrofluoroether	[31]
Immersion cooling with fin structures	Cylindrical	Direct	Oil	[32]
Immersion cooling	Cylindrical	Direct	Mineral oil	[33]
Immersion cooling	Prismatic	Direct	Mineral oil	[34]
Immersion cooling	Prismatic	Direct	Hydrofluoroether	[35]
Manifold channel immersion cooling	Prismatic	Direct	Deionized water	[36]
Immersion cooling with graphic fins	Prismatic	Direct	Hydrofluoroether	[37]
Immersion cooling	Prismatic	Direct	Silicone oil	[38]

B. Heat Transport

1. Pumps

Since the SUSAN TMS primarily uses single-phase liquid cooling, pumps are one of the primary power consumers and mass contributors. The pump KPPs are therefore defined as efficiency and specific power. Data was collected from product datasheets for 26 pumps from 9 different vendors specific to aeronautic, aerospace, and automotive applications. These included coolant, oil, refrigerant, water, and fuel pumps. Only electrically-driven non-submersible pumps were considered. For the efficiency KPP, the end-to-end efficiency was calculated including motor and motor controller (if applicable) losses. From this dataset, the best performing pumps had efficiencies around 0.50. This is chosen as the TRL 5+ KPP, with projections of 0.55 for TRL 3-4 and 0.60 for TRL 1-2.

Specific power is defined as the rated output power divided by the total mass of the pump package, including drive motor, motor controller, accumulator, and valves if applicable. For this calculation, specific power was scaled by the

number of pumps for packages that contain a redundant pump. The data spanned a wide range and are correlated with the output power of the pump. Figure 4 plots the specific power as a function of output power and shows that the data can be correlated by a power law of 11.8 $P^{0.3448}$ where P is the output power. To characterize the best performing pumps, and project to future technology developments, this power law is scaled up by increasing the coefficient. The TRL 5+ line in Fig. 4 was scaled up to 15 $P^{0.3448}$ to approximately fit the higher specific powers. Similarly, the power law coefficient for TRL 3-4 and TRL 1-2 was increased to 17 and 19 respectively.

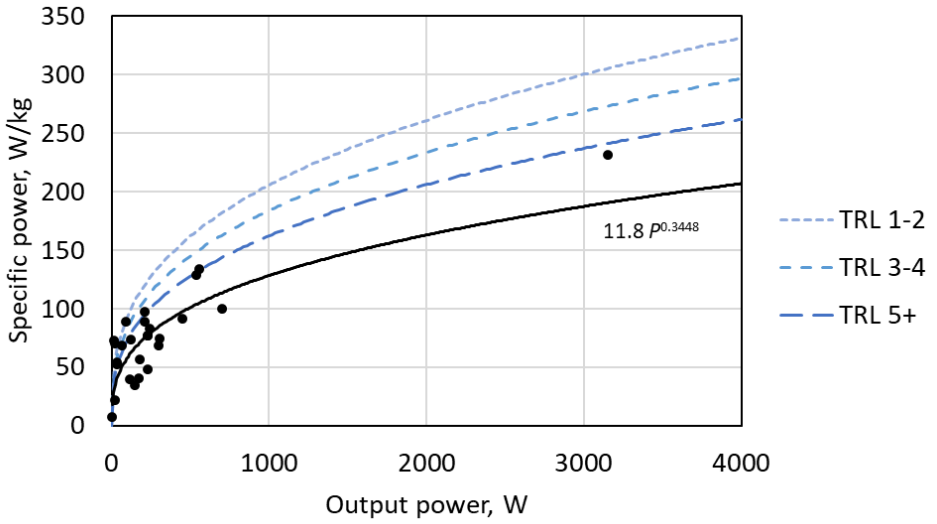

Fig. 4 Pump specific power KPP as a function of output power

2. Heat Pumps

Heat pumps are utilized in the baseline SUSAN TMS, primarily for battery module cooling on hot days on the ground where outside air temperatures are near or exceed battery temperature limits. While any type of heat pump technology is considered, the complied TRL 5+ data only include vapor compression cycles. Currently, airborne vapor cycle machines are mostly used for environmental control on regional aircraft, helicopters, and military aircraft. They are also used for galley cooling on at least two wide-body aircraft [39]. Larger vapor cycle machines for avionics and hardware cooling are primarily found on military aircraft [40]. Therefore, TRL 5+ data is somewhat limited and was sourced from 9 product specifications from 5 different suppliers.

A similar approach to fluid pumps was taken in characterizing the weight KPP. Here it is defined as specific cooling, which is the cooling capacity divided by the total mass of the heat pump. Figure 5 plots the specific cooling as a function of cooling capacity with a power law fit of 0.522 $P^{0.6216}$. The highest specific cooling designs are approximately fit with a coefficient of 0.7 and represent the TRL 5+ KPP. The power law coefficient for TRL 3-4 and TRL 1-2 are 0.8 and 0.9 respectively.

For the power consumption KPP, coefficient of performance (COP) was chosen, defined as the ratio of the cooling capacity of the heat pump to the power input. Public COP data for state-of-the-art airborne heat pumps is also scarce, but COPs in the range of 1 to 2 were reported for one military aircraft [41]. COPs for lower TRL heat pumps exceed 9 for vapor cycle and other refrigeration technologies [42–46]. For this study, values of 2.0, 4.0, and 6.0 were chosen for the TRL 5+, TRL 3-4, and TRL 1-2 KPPs respectively.

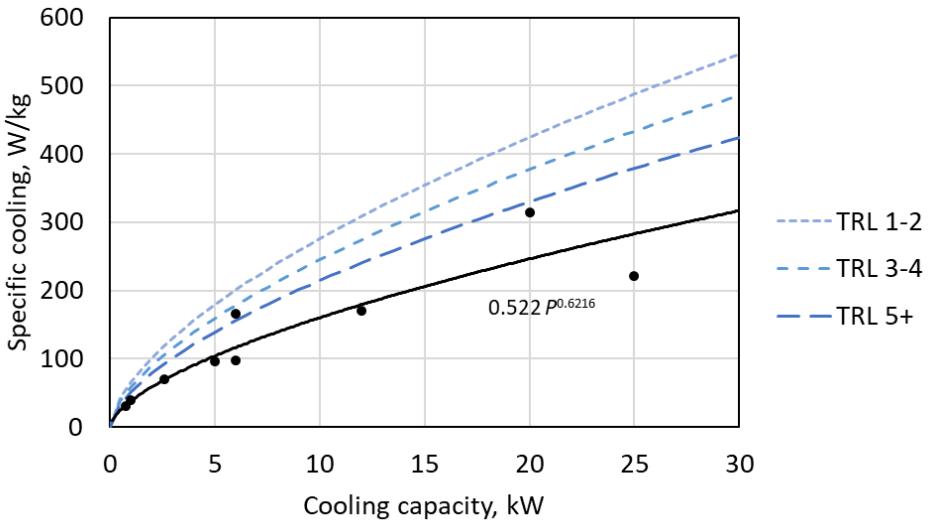

Fig. 5 Heat pump specific cooling as a function of cooling capacity

C. Heat Rejection

Primarily, liquid/air heat exchangers are utilized for heat rejection since ambient air is the primary heat sink for the SUSAN TMS. Heat exchanger effectiveness is chosen as the thermal KPP, which is defined by Eq. 3

$$\varepsilon_{HX} = \frac{T_{1,out} - T_{1,in}}{T_{2,in} - T_{1.in}} \tag{6}$$

where the subscript 1 refers to the fluid with the smaller heat capacity rate (typically air) and 2 refers to the fluid with the larger heat capacity rate (typically coolant). Similar to the heat acquisition KPPs, the ratio of heat load to pumping power and heat load to drag power are used for the fluid KPPs. Drag power is defined as the product of the air-side volumetric flow rate and the air-side pressure drop across the heat exchanger core. Similar to heat pumps, specific rejection, the ratio of heat rejected to heat exchanger mass, is chosen for the weight KPP.

TRL 5+ data was collected across multiple operating points for 18 different heat exchangers from several different manufacturers. All heat exchangers were of the plate-fin type and were designed for aeronautical applications. Coolants included oil, water, and glycol/water mixtures. Lower TRL data was also collected for additively manufactured and triply periodic minimal surface (TPMS) heat exchangers [47–49], however complete data was limited as many such studies do not report mass or liquid side pressure drop.

Since the weight, fluid, and thermal performance of a heat exchanger are interconnected and impact each other, the four KPPs are plotted in Fig. 6. The fluid performance for the air side and the liquid side are indicated by the horizontal and vertical axes respectively. The shaded region encompasses the range of fluid KPP values spanned by the dataset. The best performing designs in terms of these two KPPs lie toward the upper right of the graph.

The weight KPP is represented on the graph by lines of constant specific heat rejection. These indicate the approximate weight KPP values based on the data for the highest specific rejection designs at a given coordinate of the two fluid KPPs. Overall, the best performing designs in terms of the weight KPP lie toward the lower left of the graph. This reveals the general trend that lower pressure drop and lower drag heat exchangers will tend to be heavier, and vice versa. The thermal KPP is represented on the graph by lines of constant effectiveness, using the same approach as the weight KPP. This data indicates that effectiveness is less correlated with specific rejection and heat load per pumping power, and more correlated with heat load per drag.

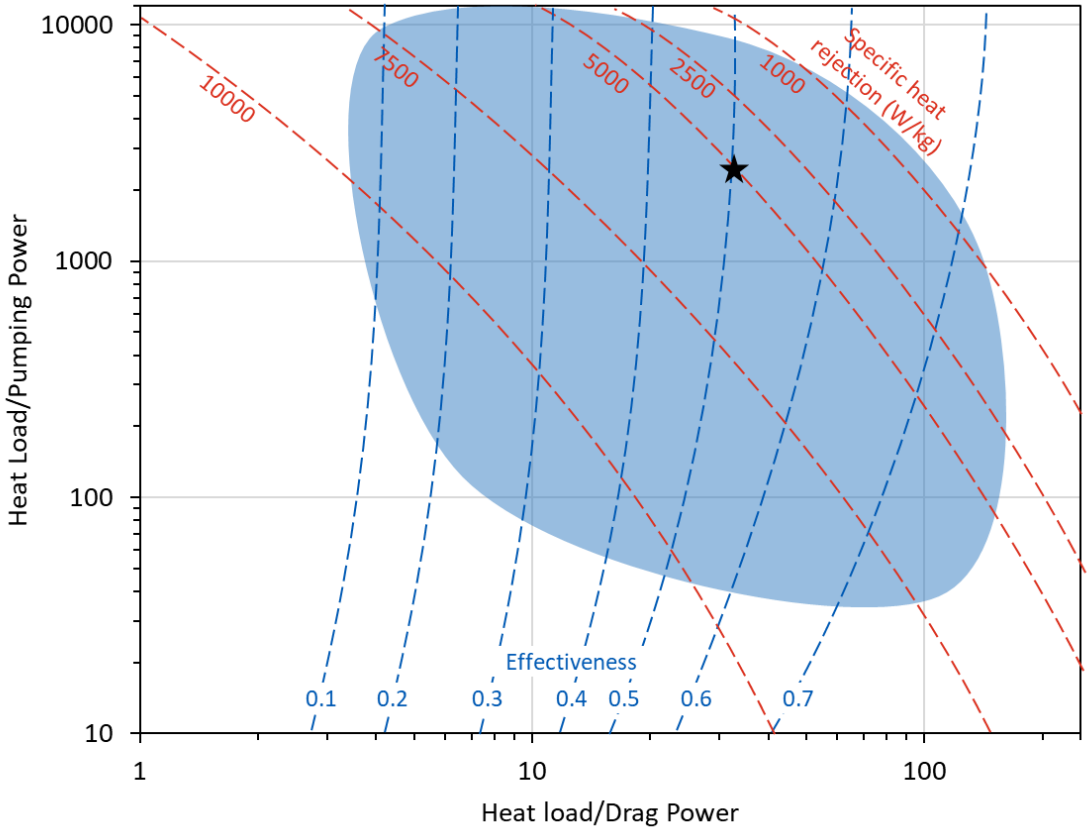

Fig. 6 Heat exchanger KPPs for TRL 5+

As with the heat acquisition KPPs, the ideal set of heat exchanger KPPs will depend on the TMS architecture, mission profile, etc. At the TRL 5+ level, that point may lie anywhere in the shaded region of Fig. 6. For the SUSAN thermal analysis, the selected TRL 5+ KPPs are indicated by a star (★). Values are summarized in Table 5. Recent studies suggest that additively manufactured heat exchangers can improve thermal performance at the cost of air-side pressure drop and mass [48,50]. Therefore, for the TRL 3-4 KPPs, effectiveness and heat load per pumping power are increased while specific rejection and heat load per drag power remain at the TRL 5+ levels. For future technology development, it is projected that advancements will lead to mass savings compared to the state of the art [51,52], so all values are increased for the TRL 1-2 KPPs.

D. Key Performance Parameter Summary

A summary of all the KPPs and their selected values for the SUSAN TMS sizing and analysis is provided in Table 5. With this set of parameters, high-level TMS performance can be modeled and weight, power draw, and drag impacts can be quantified. These values may also inform performance goals for component-level technology development for SUSAN and other electrified aircraft thermal management systems.

Table 5 Thermal Management System Key Performance Parameters

	TRL 5+	TRL 3-4	TRL 1-2	Unit	TRL 5+	TRL 3-4	TRL 1-2	Unit	TRL 5+	TRL 3-4	TRL 1-2	Unit	TRL 5+	TRL 3-4	TRL 1-2	Unit
	Cooling Effectiveness				Heat Load/Pumping Power											
Heat Acquisition																
Motors/Generators	0.20	0.27	0.32	-	2.5E2	5.0E2	1.0E3	-								
Converters	0.12	0.26	0.33	-	2.5E3	1.0E5	4.0E5	-								
Batteries	0.70	1.80	2.10	-	1.0E5	1.0E6	2.0E6	-								
Circuit Interrupters	0.12	0.26	0.33	-	2.5E3	1.0E5	4.0E5	-								
	Efficiency | COP				Specific Power | Rejection											
Heat Transport																
Pump	0.50	0.55	0.60	-	$15P^{0.3448}$	$17P^{0.3448}$	$19P^{0.3448}$	W/kg								
Refrigeration	2.0	4.0	6.0	-	$0.7P^{0.6216}$	$0.8P^{0.6216}$	$0.9P^{0.6216}$	W/kg								
	Effectiveness				Heat Load/Pumping Power				Heat Load/Drag Power				Specific Heat Rejection			
Heat Rejection																
Ram Air HX	0.50	0.60	0.70	-	2500	3000	3500	-	33	33	46	-	5.0E3	5.0E3	7.0E3	W/kg

IV. SUSAN TMS Design

The SUSAN TMS primarily utilizes single-phase liquid cooling, rejecting to the outside air using a combination of ram-air and skin (or outer-mold-line) heat exchangers. On hot days, additional heat rejection is provided by a heat pump during taxi, takeoff, and climb. The TMS layout is shown in Fig. 7. Heat acquisition is through direct immersion cooling, wherein the coolant makes direct contact with current carrying devices, such as motor windings, power electronics, circuit boards, and bus bars. This method of cooling provides sufficient heat transfer to handle the large heat fluxes generated by the high power density components and requires a dielectric coolant. For the purposes of the fluids and thermal analyses in this paper, the coolant is assumed to have the thermophysical properties of a polyalphaolefin (PAO) from MIL-PRF-87252E [53].

A unique feature of the TMS is that a significant portion of the heat transport is done via liquid-cooled electrical lines, both AC and DC. This integration of the electrical and thermal distribution systems is predicted to be a net weight savings [54,55]. The benefits are greater for longer lengths of lines, therefore this technology is only employed for the AC lines running from the tail of the aircraft to the wings, and within the DC busses. Lines that are predicted to be shorter, such as between motors/generators and their respective converters, are not liquid cooled. Implementation of this design creates an even tighter coupling of an already highly integrated thermal and electrical system that is typical for EAP. The electrical components must be placed on the fluid loops in roughly the same relative positions as they are on the AC and DC circuits. For example, the coolant loop that primarily services the electric engine components (MGC, EEM, EEMC, batteries, and DCDC) is configured with four parallel branches since these components are also in parallel on the DC bus. In Fig. 7 the liquid-cooled electrical lines are represented by hollow arrows, while fluid-only lines are represented by solid arrows.

Another advantage of this approach is that the redundancy and fault tolerance of the distributed electric propulsion is maintained in the TMS. For example, a failure in a single wing coolant loop will not impact thermal management of components on the other wing or tail coolant loops. This redundancy in the TMS is an important factor to consider in the weight, power draw, and drag of a realistic hybrid-electric aircraft. This one loop per propulsor design aligns with typical oil cooling systems for fuel-burning aircraft engines, where each engine on an aircraft has its own coolant loop, pump, and heat exchanger. Such systems often use two pumps per engine; the SUSAN TMS only uses one pump per loop since the system is already highly redundant. Redundancy is indicated in Fig. 7 where each shaded box is a repeated unit. There are a total of 21 loops: 16 that primarily service the wing electric engines (plus the AC lines, breakers, and four turbine control converters), 4 that service each motor/generator in the tail, and 1 that services the turbine control motor/generator in the tail. The 16 wing loops also interface with the heat pumps via additional pumped fluid loops.

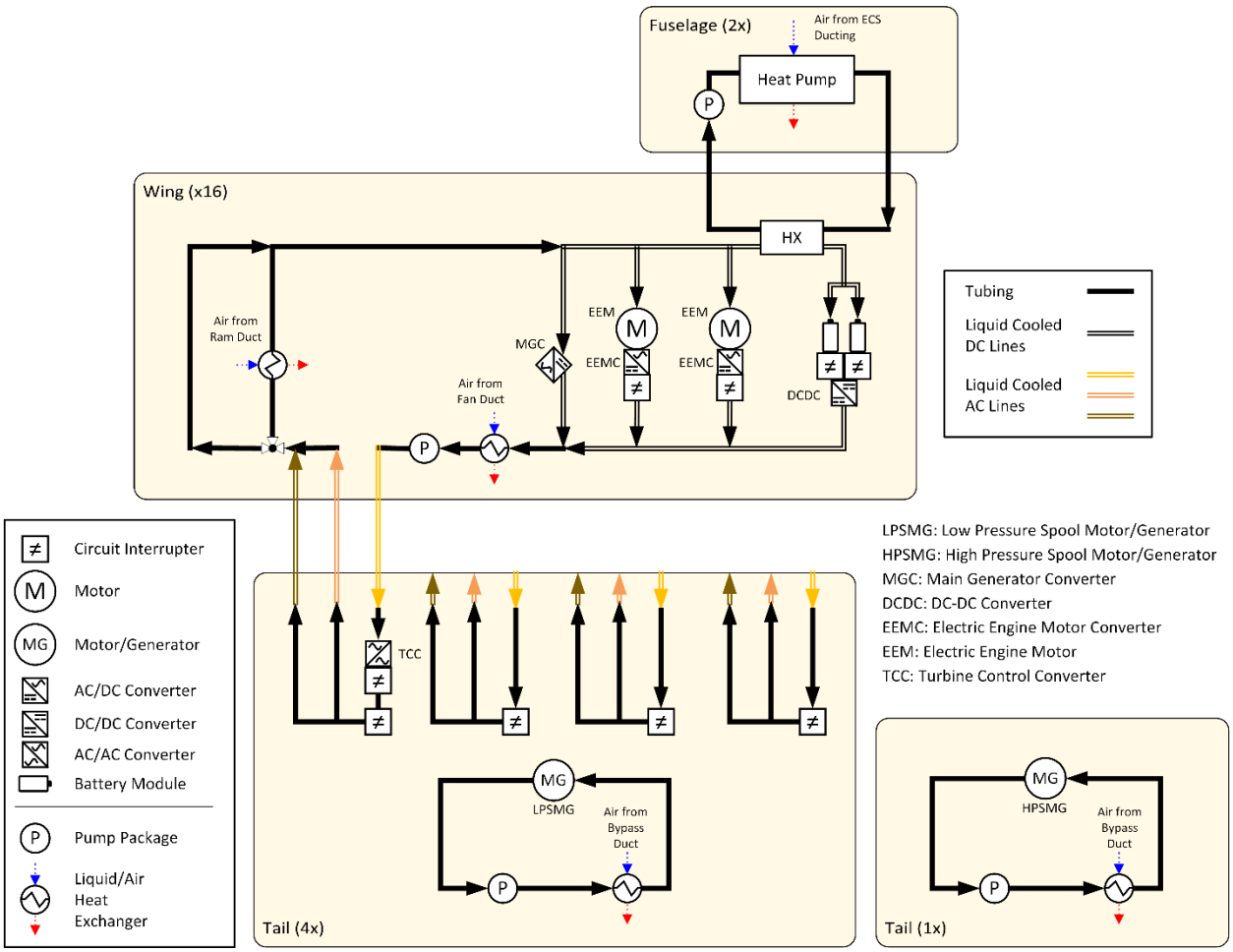

Fig. 7 SUSAN TMS diagram

As was mentioned previously, heat pumps are primarily needed for battery module cooling on hot days on the ground where outside air temperatures are near or exceed battery temperature limits. The batteries will likely be located in unpressurized compartments in the wings or fuselage where conditioned air is not available. Typical battery temperature limits range from 40 °C to 60 °C, while outside air temperatures can be up to 49 °C, for example, on a 1% Hot Day at sea level [56]. Additionally, many current aircraft are certified to take off in outside air temperatures ranging from 50 °C to 60 °C [57]. Other solutions may be considered in future trade studies, such as pre-cooling the batteries, adding additional heat sinks like phase change materials, or using evaporative coolers. However, these solutions are dependent on the available thermal mass and would need to be sized based on the time duration between disconnection from ground cooling and arrival at an altitude where the outside air is cooler. According to the FAA's Aviation System Performance Metrics database, for over 10 million US flights recorded in 2023, the average taxi out time was about 17 minutes and the average taxi in time was about 8 minutes. In 2.6% of those flights the taxi out time was greater than 40 minutes, and in 0.56% of those flights (over 60,000 flights) the taxi out time was greater than an hour. A heat pump is expected to trade better on mass for longer duration cooling requirements.

For heat rejection, each coolant loop rejects to one or more liquid-air heat exchangers. The wing loops utilize a ducted ram-air heat exchanger, notionally located local to each electric engine on the wing. Additionally, OML heat exchangers are positioned in the fan duct, downstream of the fan, which provide some heat rejection during taxiing when the fans are running. The 5 tail loops reject to non-OML heat exchangers that are located in the bypass duct of the aft turbine engine. These also provide some heat rejection during taxiing. The heat pumps are assumed to reject to ram-air heat exchangers located within the existing ducting used for the environmental control system (ECS) heat exchangers. The ECS ducting also has existing puller fans to facilitate heat rejection during taxiing and other ground operations. For this paper, any additional power draw from the puller fans or drag from the heat pump heat exchangers are neglected. Future studies may further refine these impacts.

V. SUSAN TMS Sizing and Mission Analysis

A. Inputs

To complete a sizing and analysis of the SUSAN TMS, several inputs are needed. The KPP definitions for the EPS and TMS are needed to characterize the performance of those systems and are taken from previous work and the above Table 5 [6]. The environmental requirements are needed as boundary conditions for heat rejection. These were defined in previous work, and are defined as a 20% frequency of occurrence Cold Day and a 1% frequency of occurrence Hot Day as defined by AS210 [56,57]. These frequency of occurrence day types are shown in Fig. 8. The TMS system architecture (Fig. 7) is another needed input. The final input is the flight profile, which determines the power requirements for the EPS.

Development of the SUSAN flight profiles has been previously detailed [5,58]. A 35,000 ft design mission is shown in Fig. 9 with a 1-hour taxi out, where takeoff begins at t=0. The end of the profile includes a landing abort and diversion using reserve fuel. The power requirements derived from the flight profile are combined with the EPS efficiency KPPs to generate the component heat loads.

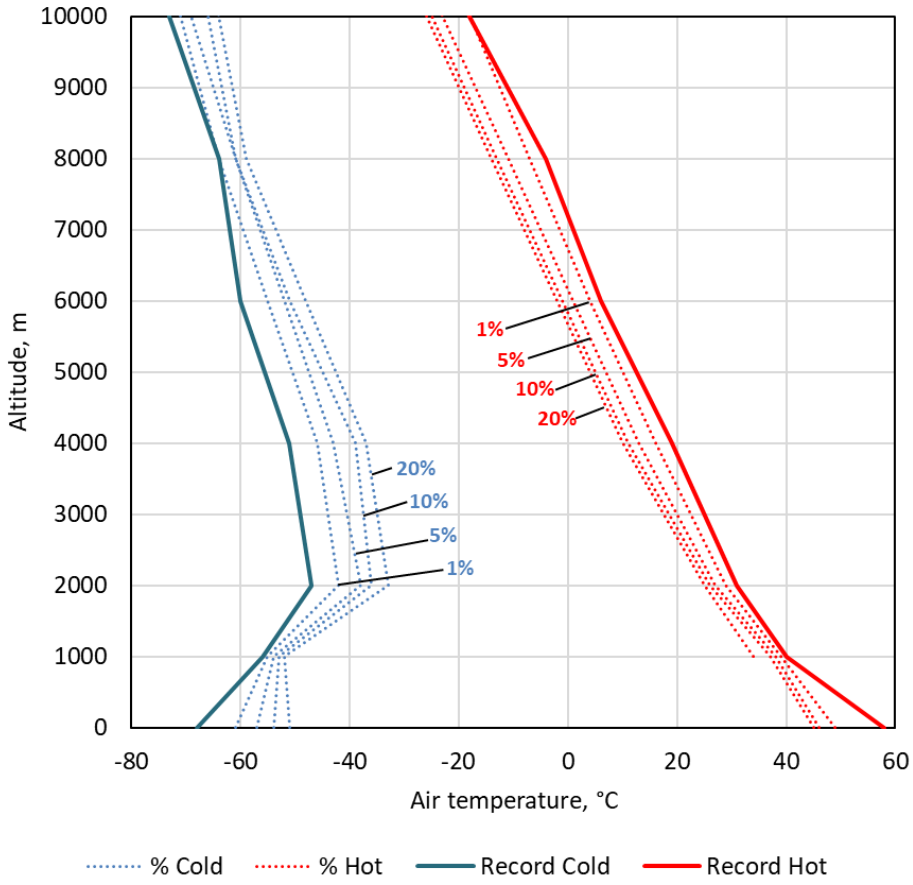

Fig. 8 Frequency of occurrence 1%, 5%, 10%, 20% and record temperatures for hot and cold days

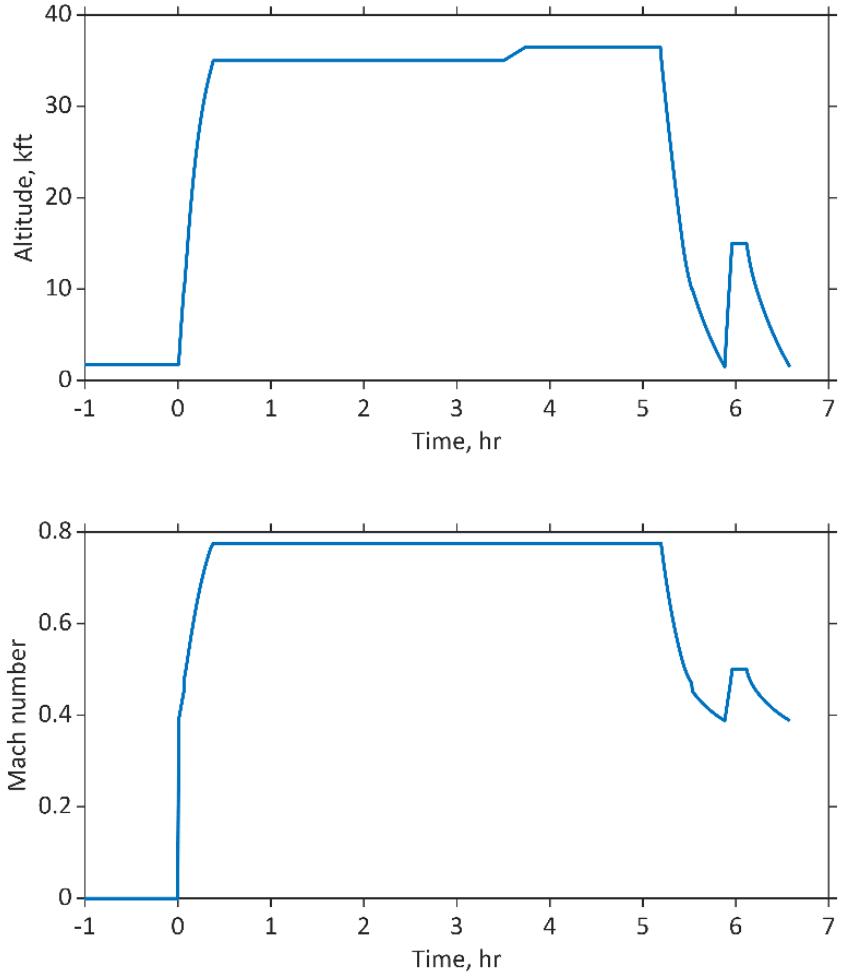

Fig. 9 SUSAN 35 kft design mission

The component heat loads used in this study were determined using a MATLAB/Simulink model of the full-scale SUSAN Power/Propulsion System [59]. The propulsion system model incorporates a zero-dimensional non-linear aero-thermal model of the aft-mounted turbofan engine and the 16 underwing electric engines built using the Toolbox for the Modeling and Analysis of Thermodynamic Systems (T-MATS) [60]. The electrical power system is modeled using the PowerFlow blockset of the Electrical Modeling and Thermal Analysis Toolbox (EMTAT) [61] and includes electric machines (motor/generators) for each of the 16 electric engines and the aft turbofan engine, inverter/converter controllers for each electric machine, and the secondary battery and DCDC converter for each electric engine. The PowerFlow blockset models each component using an efficiency map based on the component's operating condition (current/voltage or torque/speed) to determine the power losses. To determine the heat loads for each component, the Power/Propulsion System model was run through simulated flight profiles drawn from the SUSAN trade studies. The power lost through each component is assumed to be entirely converted to heat that must be removed from the system.

The resulting total heat loads are shown in Fig. 10 for each KPP level. Peak loads occur at takeoff and go-around (0.7 MW for TRL 1-2, 1.3 MW for TRL 3-4, 3.2 MW for TRL 5+). Since these coincide with the lowest altitudes and highest outside air temperatures, they are the sizing point for the heat exchangers and pumps. Since the heat pump is primarily needed during ground operations, its sizing point based on the loads during taxi (0.14 MW for TRL 1-2, 0.27 MW for TRL 3-4, 0.63 MW for TRL 5+). A breakdown of the loads by component for a single electric engine coolant loop is shown in Figs. 11-13 for each KPP level. Due to their length, the AC cables make up the largest fraction of the total heat load.

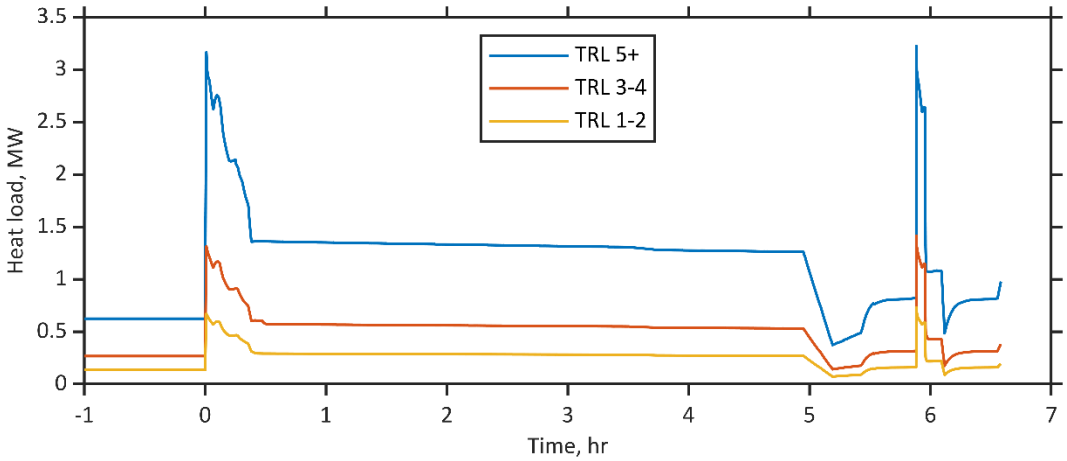

Fig. 10 Total heat load for all components at each EPS KPP level

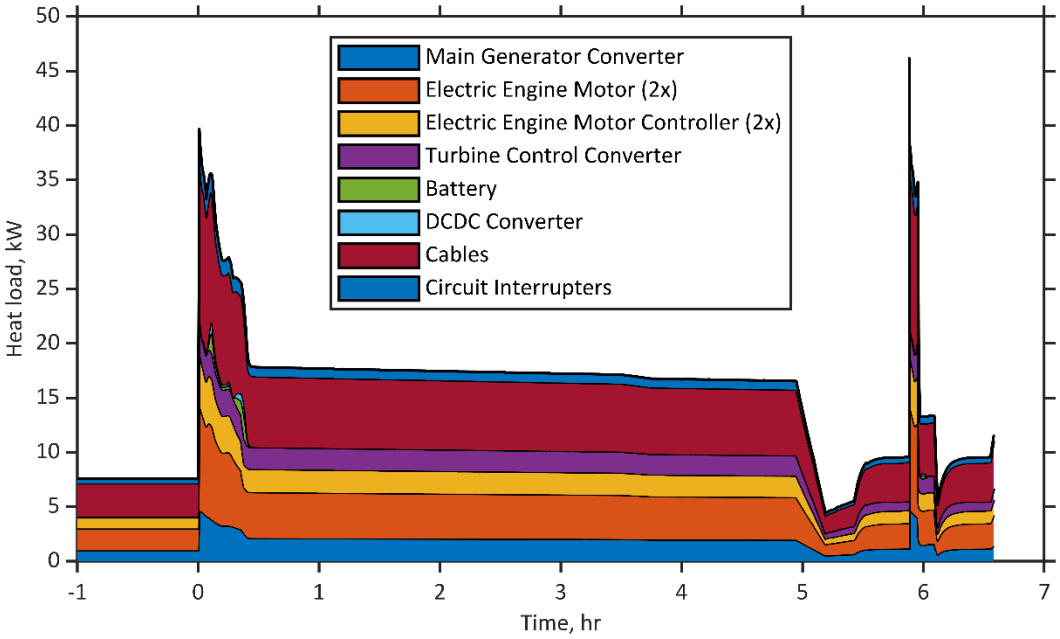

Fig. 11 Component heat loads for a single electric engine coolant loop, TRL 1-2 KPP level

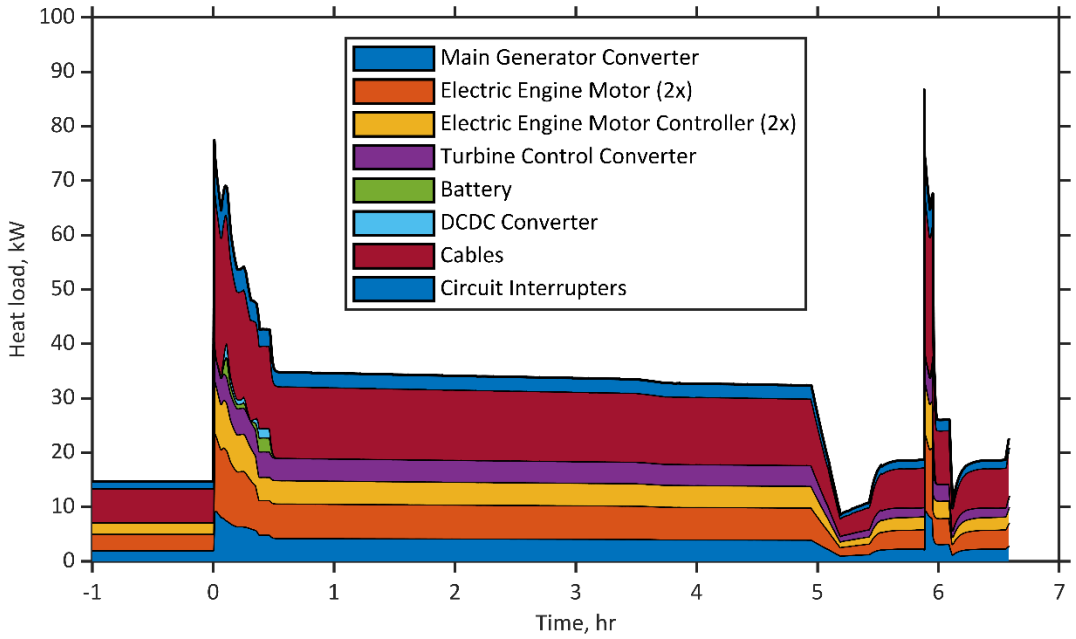

Fig. 12 Component heat loads for a single electric engine coolant loop, TRL 3-4 KPP level

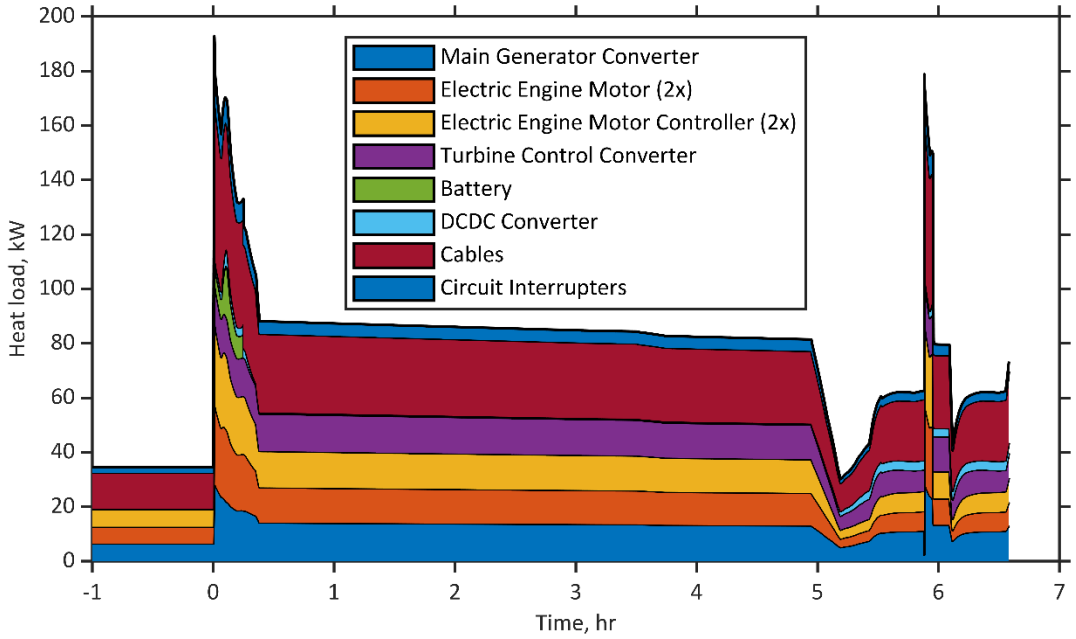

Fig. 13 Component heat loads for a single electric engine coolant loop, TRL 5+ KPP level

B. SUSAN TMS Sizing

Having defined the above inputs, the TMS can be sized and the mass, power draw, and drag can be calculated for the sizing point. As mentioned above, the sizing point is the peak load during takeoff. The required flow rates for each component are calculated from the KPPs, heat loads, and desired inlet and component temperatures. A 25% margin is applied to all heat loads based on guidelines from standards and best practices [57] and since these heat loads are one of the larger sources of uncertainty. The desired battery module inlet temperature is chosen to be 40 °C. The desired inlet temperature for all other components is chosen to be 70 °C based on the expected achievable outlet temperature

for the heat exchangers. For a sea level takeoff on a 1% Hot Day, the outside air temperature is 49 °C. At takeoff speeds the static air temperature directly upstream of the heat exchangers can be as high as 59 °C, assuming stagnation. Therefore, 70 °C is chosen as an achievable coolant outlet temperature for the heat exchangers. The OML heat exchanger in the electric engine fan duct is neglected for simplicity. The desired component temperatures are chosen to be the maximum temperature limit of each component. For this sizing, the limits across all KPP levels are 200 °C for motors/generators, 175 °C for converters and circuit interrupters, and 60 °C for battery modules. These limits could be considered to be an additional KPP or a parameter for future trade studies.

During the sizing procedure, it was found in some cases that the calculated flow rates for the electric engine coolant loop components were not high enough to produce the desired heat exchanger outlet temperature of 70 °C. Therefore, flow rates were increased by lowering the desired converter temperatures until the heat exchanger outlet reached 70 °C. Converters were specifically chosen since each parallel branch of the electric engine loops services a converter, so the flow rate of each branch is affected by the required converter flow rate. The desired converter temperature for each KPP level was found to be 125 °C for TRL 1-2, 110 °C for TRL 3-4, and 120 °C for TRL 5+.

After the flow rates are calculated, pressure drops through all components and heat exchangers are subsequently determined. Using the KPPs, the pump input power and mass can be calculated. Heat exchanger mass and drag are also calculated from the heat loads and KPPs, while heat pump mass and input power are calculated from the taxi heat loads and KPPs. The culmination of these calculations is the total mass, power consumption, and drag at takeoff values recorded in Table 6 for each KPP level.

From the table, it is seen that the total mass is roughly halved moving from a lower performing KPP level to the next highest (e.g. from TRL 5+ to TRL 3-4). This is due to a combination factors, namely the decrease in heat loads with higher efficiencies and the increase in TMS component specific rejection and specific power as the level of technology improves beyond the state of the art. A mass breakdown of the TMS by component is shown in Fig. 14. Heat exchanger mass makes up the largest fraction of the total TMS mass for the TRL 3-4 and TRL 5+ KPP levels; however, at the TRL 1-2 level, heat pumps comprise the majority of the TMS mass. Because the fan duct OML heat exchangers were neglected in this sizing study and will also provide heat rejection during taxiing, the calculated heat pump mass is expected to be slightly overestimated.

One fact remains true for all KPP levels: power consumption at takeoff is nearly entirely due to the heat pumps operating on a 1% Hot Day. On days with cool enough outside air temperatures on the ground, the heat pumps would not need to be activated for taxiing. Additionally, after ascending to altitudes where the outside air is cooler, the heat pumps can be deactivated and the TMS power consumption reduces to the draw from the fluid pumps.

Similar to the trends observed with mass and power, the total drag of the system is also reduced by a factor of 2 to 3 when moving across KPP levels. It is worth noting again that the drag KPP was based on core drag only. Additional drag due to inlets and ducting are not considered. Thrust due to the ramjet or Meredith effect is also not included and may significantly offset the core drag [62–65].

Table 6 SUSAN TMS mass, power, and drag from sizing study

	Mass, kg	Heat pump power consumption at takeoff, kW	Fluid pump power consumption at takeoff, kW	Drag power at takeoff, kW
TRL 1-2	264	23	1	16
TRL 3-4	528	68	4	43
TRL 5+	1273	315	19	129

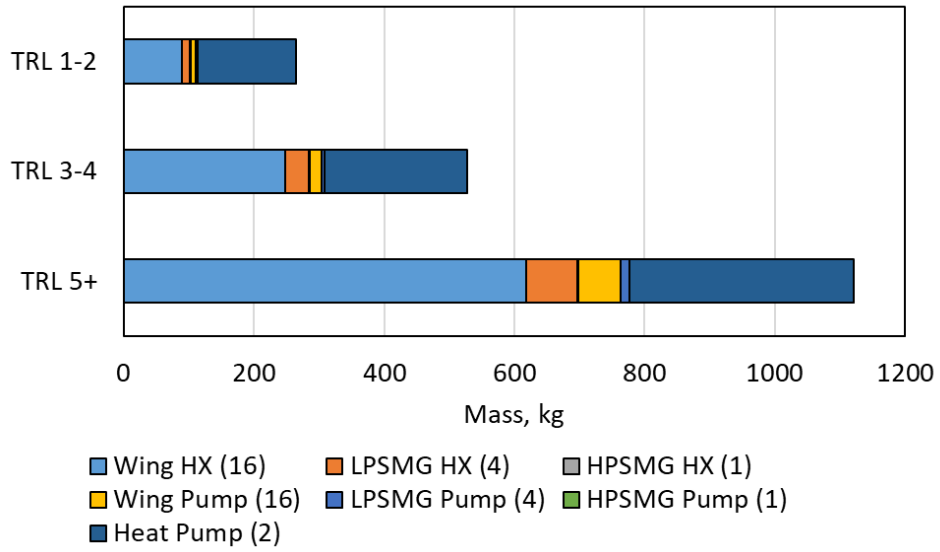

Fig. 14 SUSAN TMS mass breakdown from sizing study

C. SUSAN TMS Modeling Setup

An analytical model of the SUSAN TMS was developed to study the transient performance over the course of an entire flight profile. This model also serves as a refinement of the sizing study presented in the previous section, providing a higher fidelity representation of the OML heat exchangers, the thermal mass of components, and the thermal and fluid performance of the piping system including the liquid-cooled electrical lines. This model was developed in Thermal Desktop 6.1 as a 1-dimensional thermal/fluid network and is shown in Fig. 15 following a similar layout as Fig. 7. For simplicity, only one type of each coolant loop is modeled: a wing loop with turbine control converter (TCC), a wing loop without TCC, a tail loop servicing the low-pressure spool motor/generator, and a tail loop servicing the high-pressure spool motor/generator.

KPPs from Table 5 are converted into conductances and loss coefficients (K factors) for all components. Pipe losses are calculated using a Darcy friction factor and estimates of the pipe lengths. Heat loads for the liquid-cooled electrical lines are applied uniformly along the length of the line. As previously mentioned, the AC lines make up a large portion of the total heat load; their length is estimated as 15 m, as they must run from the tail of the plane out to the wings. Component heat loads are modeled without the 25% margin for sizing. Pump flow rates are fixed based on the flow rates calculated from the sizing study.

The freestream air boundary conditions of temperature, pressure, and density defined from the frequency of occurrence day types. The air properties at the face of the ram-air heat exchangers are assumed to be at stagnation. Air properties at the OML heat exchangers in the electric engine fan ducts, as well as the tail heat exchangers in the turbofan bypass duct, are calculated from the freestream properties, duct geometry, and Mach number outputs from the T-MATS model that was used to generate the heat loads.

Thermal mass (capacitance) is calculated for the motors/generators and battery modules. First, the mass is calculated based on the EPS KPP of specific power. For motors/generators, this total mass is then scaled to 14% and assigned the properties of copper to approximate of the fraction of copper in a motor, as windings are a primary heat source. Similarly, the battery module mass is calculated and scaled to 79% to approximate the fraction of battery cell mass in a module. The battery module specific heat is 959 J/kg/K and density is 2293 kg/m^3. Converters and circuit breakers are assumed to have zero capacitance since power electronic devices respond very quickly to changes in heat load.

Initial conditions are steady-state operation during taxiing. As shown in Fig. 9, the airplane is stationary (M=0) and is therefore reliant on the heat pump and fan duct and bypass duct heat exchangers for cooling. Heat pump performance is not explicitly modeled, but the required cooling capacity to maintain the battery module inlet temperature at 40 °C is calculated.

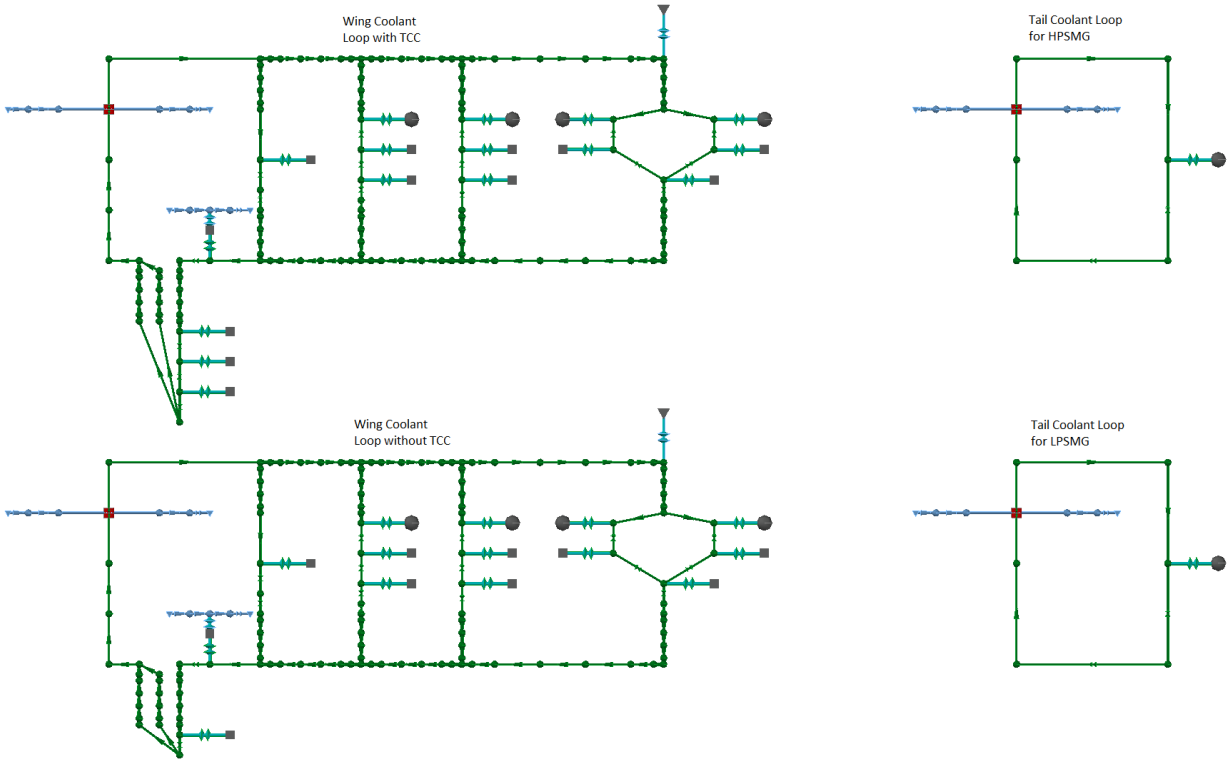

Fig. 15 SUSAN TMS Thermal Desktop model

D. SUSAN TMS Modeling Results

1. Taxi Results

Component temperatures during steady-state taxi are summarized in Table 7. For many of the electric engine components, the TRL 5+ TMS temperatures are somewhat lower than those in the other KPP levels. This is because a larger proportion of the total coolant flow is directed to the battery and DCDC converter branch based on the sizing study. Since the heat pump is also on this branch, the overall coolant loop temperatures are lower, but the required heat pump cooling capacity is significantly higher. This is reflected in Fig. 16 which shows the total heat rejection during taxi for each KPP level broken down into rejection to the OML heat exchangers and rejection via the heat pumps. The TRL 5+ TMS rejects around 550 kW of heat, with only 1% of that heat being rejected through the OML heat exchangers. The lower TRL TMSs, on the other hand, have less total heat to reject, and a larger fraction of that heat is rejected through the OML heat exchangers. Consequently, the heat pumps are much smaller for these KPP levels. The resulting total heat pump mass for each KPP level is 126 kg for TRL 1-2, 192 kg for TRL 3-4, and 327 kg for TRL 5+. These masses are lower than what was calculated for the sizing study in Fig. 14, since the heat rejection through the OML heat exchangers is accounted for in the thermal model. Similarly, the required heat pump input powers are lower than predicted by the sizing study: 14 kW for TRL 1-2, 48 kW for TRL 3-4, and 275 kW for TRL 5+.

Table 7 Component temperatures during steady state taxi

		KPP level		
		TRL 1-2	**TRL 3-4**	**TRL 5+**
Electric Engine Loop (with TCC)	MGC	91.6	96.3	60.2
	EEM	94.8	96.6	55.6
	EEMC	92.2	96.3	59.7
	Battery	40.3	40.4	40.4
	DCDC	40.3	40.6	40.4
	TCC	80.2	87.8	50.2
Electric Engine Loop (without TCC)	MGC	91.4	96.1	60.2
	EEM	94.6	96.4	55.5
	EEMC	92.1	96.1	59.6
	Battery	40.3	40.2	40.4
	DCDC	40.3	40.3	40.4
LPSMG		103.8	103.8	105.5
HPSMG		77.9	77.9	77.9

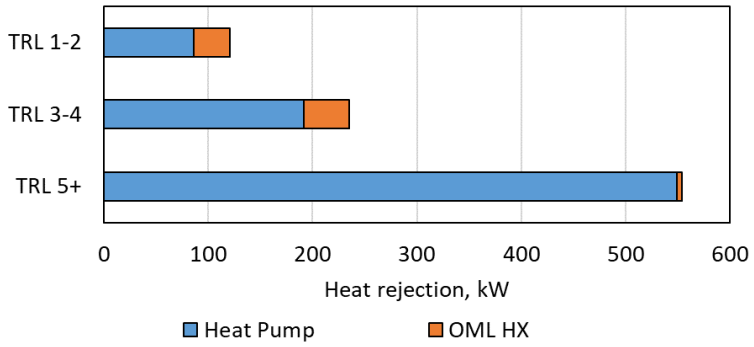

Fig. 16 Heat rejection during steady state taxi

2. In-Flight Results

Component temperatures as a function of time for the flight profiles are plotted in Fig. 17. Generally, the components are hottest at takeoff and go-around, and are coolest during descent prior to go-around. Temperatures are maintained within component limits for all KPP levels throughout the whole flight. During cruise, components on the electric engine loops (MGC, EEM, EEMC, and batteries) stay within 20 °C to 60 °C. This analysis assumes that pump flow rates are constant throughout the whole flight. Feedback control of pump flow rates could be utilized during cruise to achieve lower component temperatures. Conversely, the pump speed could be decreased during cruise to reduce power consumption as there is significant margin to component temperature limits.

To quantify the impact of the OML heat exchangers, heat rejection throughout the flight is plotted in Fig. 18 for a single electric engine coolant loop at the TRL 3-4 KPP level. As previously seen in Fig. 16, the OML heat exchanger makes up a non-negligible fraction of the total heat rejection during taxi, which reduces the cooling capacity required of the heat pumps. However, during the rest of the flight when the ram-air cooling is available, the OML rejection is minimal. The figure also illustrates that the heat pump provides some rejection during takeoff and go-around, as well as during descent. In this analysis, the heat pump is enabled when the coolant temperatures upstream of the battery rise above 40 °C. A more sophisticated control scheme may be able to reduce the duration of heat pump activation and thereby its power consumption.

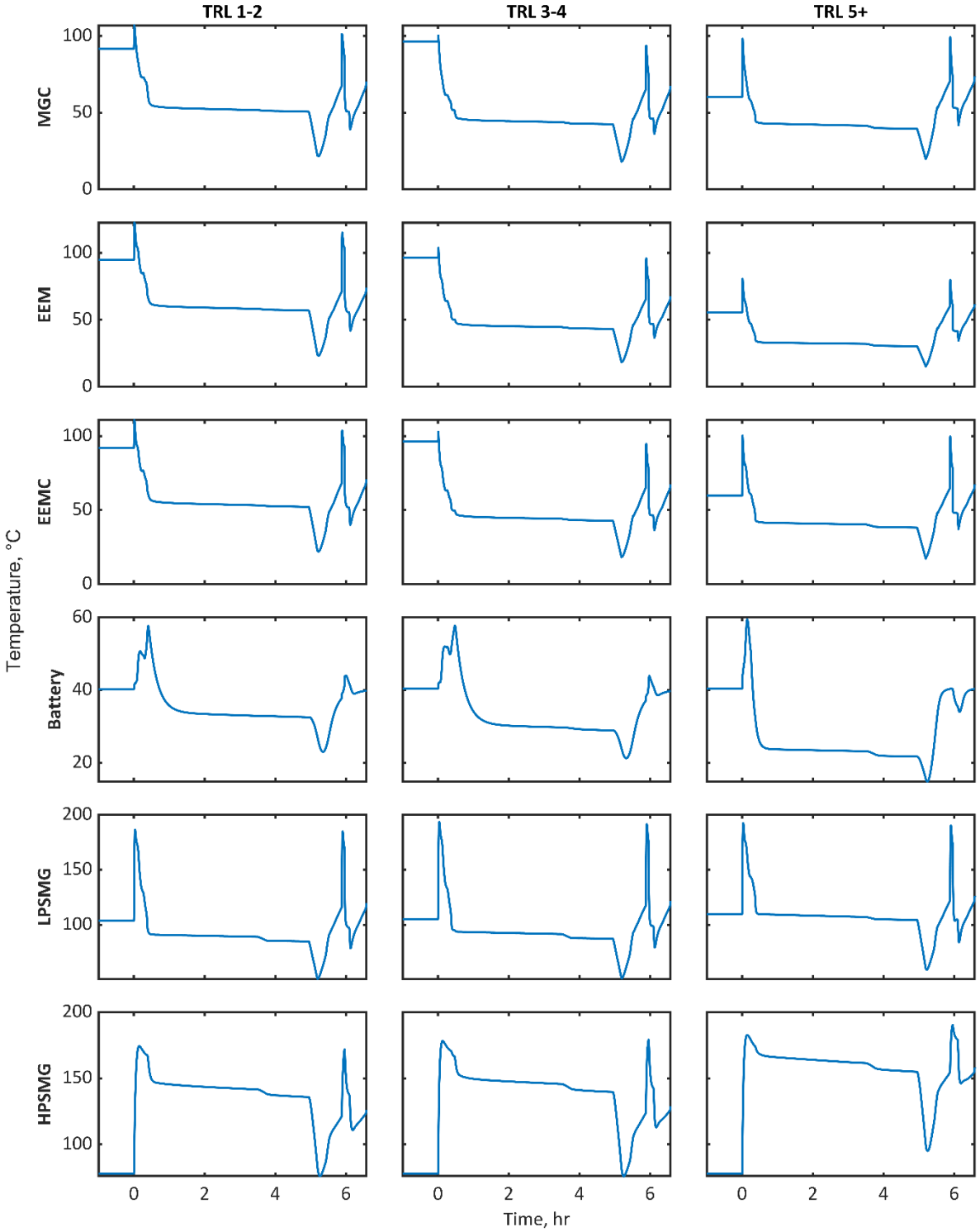

Fig. 17 Component temperatures as a function of time for all KPP levels

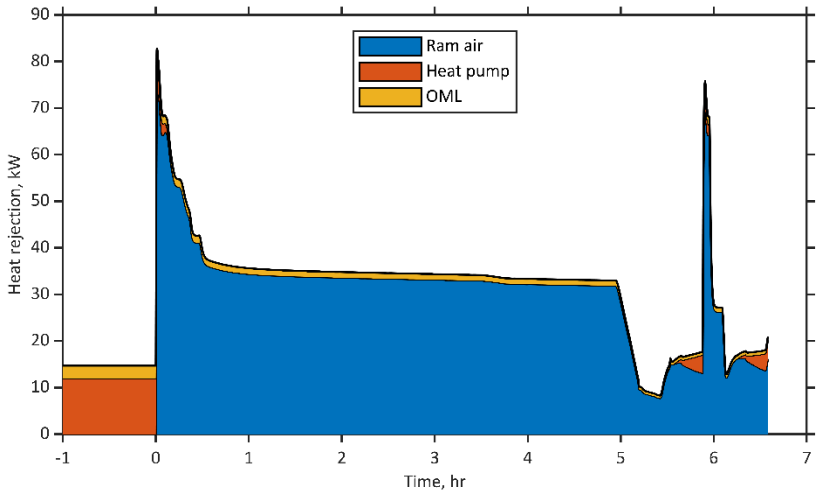

Fig. 18 Heat rejection as a function of time for TRL 3-4

Total power consumption over the flight profile is shown in Fig. 19. During taxi, the power consumption for TRL 1-2 and TRL 3-4 are less than calculated from the sizing study in Table 6. Again, this is because the OML heat exchangers are included in the model which lowers the cooling capacity required by the heat pumps. However, the TRL 5+ power consumption is much higher than predicted in the sizing study. This is due to the modeling of pressure drops in the piping systems, which was not accounted for in the sizing. Due to higher flow rates required by the TRL 5+ components, the required pump power is high at around 760 kW during cruise. Total drag is also plotted in and agrees fairly closely with the predictions from the sizing study. Overall mass, power consumption, and drag predictions based on this analysis are summarized in Table 8.

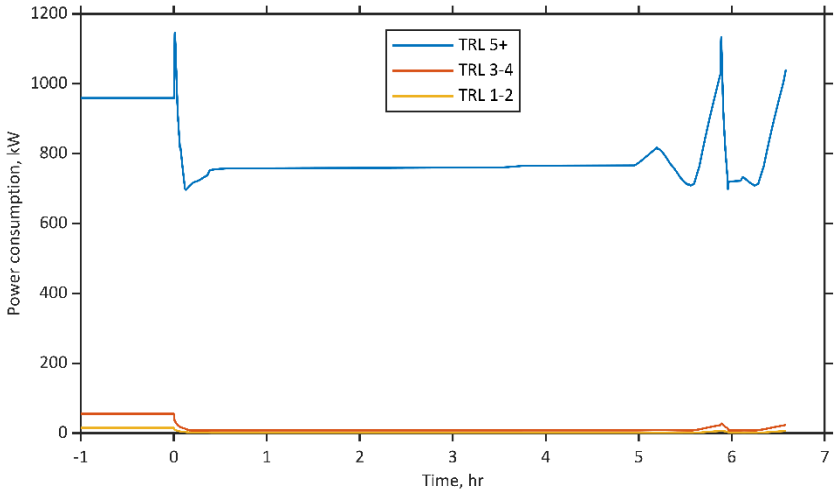

Fig. 19 Total TMS power consumption as a function of time

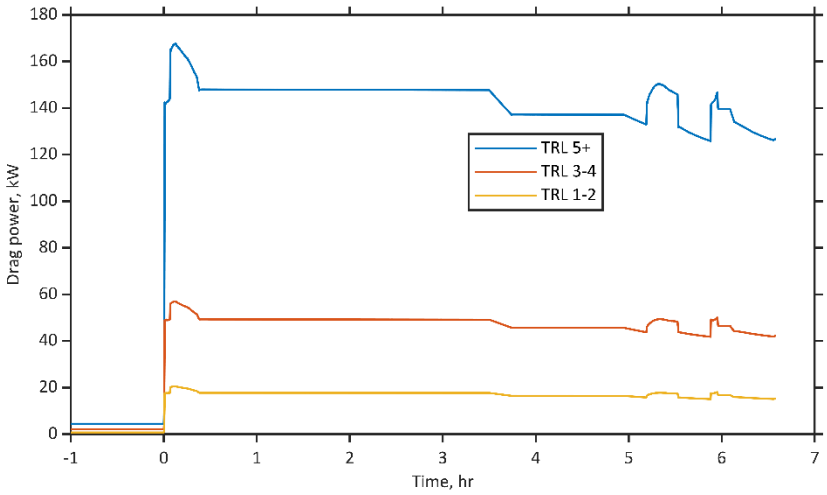

Fig. 20 Total drag as a function of time

Table 8 SUSAN TMS mass, power, and drag from thermal/fluid model

	Mass, kg	Power consumption at takeoff, kW	Power consumption at cruise, kW	Drag power at cruise, kW
TRL 1-2	239	15	1	18
TRL 3-4	501	55	8	49
TRL 5+	1155	959	760	148

VI. Conclusion

In this paper a TMS sizing and analysis methodology was described based on KPPs derived from a wide range of sources. These KPPs provide a data-driven approach to quantifying the performance of TMS components for electrified aircraft at current and future levels of technology development. Using the SUSAN aircraft as a study of a realistic highly redundant TMS, the impact of moving across the KPP levels is clear: system mass, power consumption, and drag decrease considerably as the level of technology progresses. Advancements beyond the state of the art will be necessary for large, electrified aircraft like SUSAN, as the predicted mass and power consumption may not be feasible. Future work could include development of additional KPPs to perform trade studies of technologies such as phase-change materials, oscillating heat pipes, and two-phase thermal management systems.

Acknowledgments

The authors would like to thank the Convergent Aeronautics Solutions (CAS) Project, which is part of the Transformational Aeronautics Concepts Program (TACP) in the NASA Aeronautics Research Mission Directorate (ARMD) for their sponsorship of this work.

References

[1] Coutinho, M., Bento, D., Souza, A., Cruz, R., Afonso, F., Lau, F., Suleman, A., Barbosa, F. R., Gandolfi, R., Affonso, W., Odaguil, F. I. K., Westin, M. F., Dos Reis, R. J. N., and Da Silva, C. R. I. "A Review on the Recent Developments in Thermal Management Systems for Hybrid-Electric Aircraft." *Applied Thermal Engineering*, Vol. 227, 2023, p. 120427. https://doi.org/10.1016/j.applthermaleng.2023.120427.

[2] Asli, M., König, P., Sharma, D., Pontika, E., Huete, J., Konda, K. R., Mathiazhagan, A., Xie, T., Höschler, K., and Laskaridis, P. "Thermal Management Challenges in Hybrid-Electric Propulsion Aircraft." *Progress in Aerospace Sciences*, Vol. 144, 2024, p. 100967. https://doi.org/10.1016/j.paerosci.2023.100967.

[3] van Heerden, A. S. J., Judt, D. M., Jafari, S., Lawson, C. P., Nikolaidis, T., and Bosak, D. "Aircraft Thermal Management: Practices, Technology, System Architectures, Future Challenges, and Opportunities." *Progress in Aerospace Sciences*, Vol. 128, 2022, p. 100767. https://doi.org/10.1016/j.paerosci.2021.100767.
[4] Jansen, R., Kiris, C. C., Chau, T., Machado, L. M., Duensing, J. C., Mirhashemi, A., Chapman, J., French, B. D., Miller, L., Litt, J. S., Denham, C. L., Lynde, M. N., Campbell, R. L., Hiller, B. R., Blaesser, N. J., and Heersema, N. Subsonic Single Aft Engine (SUSAN) Transport Aircraft Concept and Trade Space Exploration. Presented at the AIAA SCITECH 2022 Forum, San Diego, CA & Virtual, 2022.
[5] Chau, T., and Duensing, J. Conceptual Design of the Hybrid-Electric Subsonic Single Aft Engine (SUSAN) Electrofan Transport Aircraft. Presented at the AIAA SCITECH 2024 Forum, Orlando, FL, 2024.
[6] Haglage, J. M., Dever, T. P., Jansen, R. H., and Lewis, M. A. Electrical System Trade Study for SUSAN Electrofan Concept Vehicle. Presented at the AIAA SCITECH 2022 Forum, 2022.
[7] Sekulić, D. P., and Shah, R. K. *Fundamentals of Heat Exchanger Design*. 2024.
[8] Chattopadhyay, R., Islam, M. S., Jung, J., Mikail, R., and Husain, I. "Winding Embedded Liquid Cooling for Slotless Motors in Transportation Applications." *IEEE Transactions on Industry Applications*, Vol. 58, No. 6, 2022, pp. 7110–7120. https://doi.org/10.1109/TIA.2022.3191629.
[9] Chen, K., Feng, W., Chen, F., Lee, S., Paddock, J., Jahns, T. M., and Sarlioglu, B. Thermal Analysis of Liquid and Air Cooling of High-Power-Density Integrated Motor Drives. Presented at the 2023 IEEE Energy Conversion Congress and Exposition (ECCE), Nashville, TN, USA, 2023.
[10] Cakal, G., and Sarlioglu, B. Novel In-Core Cooling of Yokeless and Segmented Armature (YASA) Axial Flux Machines. Presented at the 2023 IEEE Energy Conversion Congress and Exposition (ECCE), Nashville, TN, USA, 2023.
[11] Chang, J., Fan, Y., Wu, J., and Zhu, B. "A Yokeless and Segmented Armature Axial Flux Machine With Novel Cooling System for In-Wheel Traction Applications." *IEEE Transactions on Industrial Electronics*, Vol. 68, No. 5, 2021, pp. 4131–4140. https://doi.org/10.1109/TIE.2020.2982093.
[12] Woodworth, A. A., Sixel, W. R., Jansen, R. H., and Szpak, G. High Efficiency Megawatt Motor Stator Thermal Performance. Presented at the AIAA AVIATION FORUM AND ASCEND 2024, 2024.
[13] Lindh, P., Petrov, I., Jaatinen-Varri, A., Gronman, A., Martinez-Iturralde, M., Satrustegui, M., and Pyrhonen, J. "Direct Liquid Cooling Method Verified With an Axial-Flux Permanent-Magnet Traction Machine Prototype." *IEEE Transactions on Industrial Electronics*, Vol. 64, No. 8, 2017, pp. 6086–6095. https://doi.org/10.1109/TIE.2017.2681975.
[14] Wanjiku, J., Ge, L., Zhang, Z., Chang, K., Wu, C., and Zhan, F. Electromagnetic and Direct-Cooling Analysis of a Traction Motor. Presented at the 2021 IEEE Energy Conversion Congress and Exposition (ECCE), Vancouver, BC, Canada, 2021.
[15] Zhang, C., Srdic, S., Lukic, S., Kang, Y., Choi, E., and Tafti, E. A SiC-Based 100 kW High-Power-Density (34 kW/L) Electric Vehicle Traction Inverter. Presented at the 2018 IEEE Energy Conversion Congress and Exposition (ECCE), Portland, OR, USA, 2018.
[16] Zhang, C., Srdic, S., Lukic, S., Sun, K., Wang, J., and Burgos, R. "A SiC-Based Liquid-Cooled Electric Vehicle Traction Inverter Operating at High Ambient Temperature." *CPSS Transactions on Power Electronics and Applications*, Vol. 7, No. 2, 2022, pp. 160–175. https://doi.org/10.24295/CPSSTPEA.2022.00015.
[17] Waye, S. K., Narumanchi, S., Mihalic, M., Moreno, G., Bennion, K., and Jeffers, J. Advanced Liquid Cooling for a Traction Drive Inverter Using Jet Impingement and Microfinned Enhanced Surfaces. Presented at the 2014 IEEE Intersociety Conference on Thermal and Thermomechanical Phenomena in Electronic Systems (ITherm), Orlando, FL, USA, 2014.
[18] Fan, J., Zhang, Z., Shah, S., Wang, J., and Agarwal, A. K. Development of Ultra High Power Density Liquid Metal Cooled Inverter. Presented at the AIAA AVIATION 2023 Forum, San Diego, CA and Online, 2023.
[19] Fan, J., Shah, S., Zhang, Z., and Wang, J. A High Performance Liquid Metal-Based Cooling System for an Ultra High Power Density Inverter. Presented at the 2023 IEEE Energy Conversion Congress and Exposition (ECCE), Nashville, TN, USA, 2023.
[20] Abramushkina, E. E., Martin, G. E., Sen, A., Jaman, S., Rasool, H., Baghdadi, M. E., and Hegazy, O. "An Innovative Additively Manufactured Design Concept of a Dual-Sided Cooling System for SiC Automotive Inverters." *IEEE Access*, Vol. 12, 2024, pp. 20454–20470. https://doi.org/10.1109/ACCESS.2024.3358685.
[21] Lee, T.-Y. "Design Optimization of an Integrated Liquid-Cooled IGBT Power Module Using CFD Technique." *IEEE Transactions on Components and Packaging Technologies*, Vol. 23, No. 1, 2000, pp. 55–60. https://doi.org/10.1109/6144.833042.
[22] Pan, D., Zhang, D., Immer, C., Dame, M., and He, J. Pump-Back Validation of a Medium Voltage High-Frequency "SiC+Si" Hybrid Three-Level ANPC Inverter for Hybrid-Electric Propulsion Application. Presented at the 2019 IEEE International Electric Machines & Drives Conference (IEMDC), San Diego, CA, USA, 2019.
[23] Moreno, G., Narumanchi, S., Tomerlin, J., and Major, J. "Single-Phase Dielectric Fluid Thermal Management for Power-Dense Automotive Power Electronics." *IEEE Transactions on Power Electronics*, Vol. 37, No. 10, 2022, pp. 12474–12485. https://doi.org/10.1109/TPEL.2022.3171744.
[24] Moreno, G., "Power Electronics Thermal Management," DOE Vehicle Technologies Program 2021 Annual Merit Review and Peer Evaluation Meeting, 2021.
[25] Yang, F., Liu, C., and Shen, J. Immersion Oil Cooling Method of Discrete SiC Power Device in Electric Vehicle. Presented at the 2022 IEEE Energy Conversion Congress and Exposition (ECCE), Detroit, MI, USA, 2022.

[26] Lai, Y., Wu, W., Chen, K., Wang, S., and Xin, C. “A Compact and Lightweight Liquid-Cooled Thermal Management Solution for Cylindrical Lithium-Ion Power Battery Pack.” *International Journal of Heat and Mass Transfer*, Vol. 144, 2019, p. 118581. https://doi.org/10.1016/j.ijheatmasstransfer.2019.118581.
[27] Liang, G., Li, J., He, J., Tian, J., Chen, X., and Chen, L. “Numerical Investigation on a Unitization-Based Thermal Management for Cylindrical Lithium-Ion Batteries.” *Energy Reports*, Vol. 8, 2022, pp. 4608–4621. https://doi.org/10.1016/j.egyr.2022.03.081.
[28] Li, W., Garg, A., Wang, N., Gao, L., Le Phung, M. L., and Tran, V. M. “Computational Fluid Dynamics-Based Numerical Analysis for Studying the Effect of Mini-Channel Cooling Plate, Flow Characteristics, and Battery Arrangement for Cylindrical Lithium-Ion Battery Pack.” *Journal of Electrochemical Energy Conversion and Storage*, Vol. 19, No. 4, 2022, p. 041003. https://doi.org/10.1115/1.4054648.
[29] Jeon, H., Hong, S., Yun, J., and Han, J. “Cooling Strategy Optimization of Cylindrical Lithium-Ion Battery Pack via Multi-Counter Cooling Channels.” *Energies*, Vol. 16, No. 23, 2023, p. 7860. https://doi.org/10.3390/en16237860.
[30] Patil, M. S., Seo, J.-H., Panchal, S., Jee, S.-W., and Lee, M.-Y. “Investigation on Thermal Performance of Water-Cooled Li-Ion Pouch Cell and Pack at High Discharge Rate with U-Turn Type Microchannel Cold Plate.” *International Journal of Heat and Mass Transfer*, Vol. 155, 2020, p. 119728. https://doi.org/10.1016/j.ijheatmasstransfer.2020.119728.
[31] Dubey, P., Pulugundla, G., and Srouji, A. K. “Direct Comparison of Immersion and Cold-Plate Based Cooling for Automotive Li-Ion Battery Modules.” *Energies*, Vol. 14, No. 5, 2021, p. 1259. https://doi.org/10.3390/en14051259.
[32] Han, J.-W., Garud, K. S., Kang, E.-H., and Lee, M.-Y. “Numerical Study on Heat Transfer Characteristics of Dielectric Fluid Immersion Cooling with Fin Structures for Lithium-Ion Batteries.” *Symmetry*, Vol. 15, No. 1, 2023, p. 92. https://doi.org/10.3390/sym15010092.
[33] Sun, Z., Guo, Y., Zhang, C., Zhou, Q., Xu, H., and Wang, C. “Algorithm-Driven Optimization of Lithium-Ion Battery Thermal Modeling.” *Journal of Energy Storage*, Vol. 65, 2023, p. 107388. https://doi.org/10.1016/j.est.2023.107388.
[34] Patil, M. S., Seo, J.-H., and Lee, M.-Y. “A Novel Dielectric Fluid Immersion Cooling Technology for Li-Ion Battery Thermal Management.” *Energy Conversion and Management*, Vol. 229, 2021, p. 113715. https://doi.org/10.1016/j.enconman.2020.113715.
[35] Li, Y., Zhou, Z., Su, L., Bai, M., Gao, L., Li, Y., Liu, X., Li, Y., and Song, Y. “Numerical Simulations for Indirect and Direct Cooling of 54 V LiFePO4 Battery Pack.” *Energies*, Vol. 15, No. 13, 2022, p. 4581. https://doi.org/10.3390/en15134581.
[36] Le, Q., Shi, Q., Liu, Q., Yao, X., Ju, X., and Xu, C. “Numerical Investigation on Manifold Immersion Cooling Scheme for Lithium Ion Battery Thermal Management Application.” *International Journal of Heat and Mass Transfer*, Vol. 190, 2022, p. 122750. https://doi.org/10.1016/j.ijheatmasstransfer.2022.122750.
[37] Choi, H., Lee, H., Kim, J., and Lee, H. “Hybrid Single-Phase Immersion Cooling Structure for Battery Thermal Management under Fast-Charging Conditions.” *Energy Conversion and Management*, Vol. 287, 2023, p. 117053. https://doi.org/10.1016/j.enconman.2023.117053.
[38] Nelson, P., Dees, D., Amine, K., and Henriksen, G. “Modeling Thermal Management of Lithium-Ion PNGV Batteries.” *Journal of Power Sources*, Vol. 110, No. 2, 2002, pp. 349–356. https://doi.org/10.1016/S0378-7753(02)00197-0.
[39] Hu, H., Sun, H., Wu, C., Wang, X., and Lv, Z. “A Steady-State Simulation Model of Supplemental Cooling System Integrated with Vapor Compression Refrigeration Cycles for Commercial Airplane.” *Applied Thermal Engineering*, Vol. 166, 2020, p. 114692. https://doi.org/10.1016/j.applthermaleng.2019.114692.
[40] Popescu, M. A. *Design and Assessment of a Novel Electrically Driven Environmental Control System for More Electric Aircraft*. Master Thesis. Delft University of Technology, 2020.
[41] Ghanekar, M. Vapor Cycle System for the F-22 Raptor. Presented at the 30th International Conference on Environmental Systems, 2000.
[42] Erkinaci, T., Coskun, F., Cotur, A., Onler, R., and Serincan, M. F. “Experimental and Numerical Investigation of a Compact Vapor Compression Refrigeration System for Cooling of Avionics in Harsh Environments.” *Applied Thermal Engineering*, Vol. 236, 2024, p. 121663. https://doi.org/10.1016/j.applthermaleng.2023.121663.
[43] Zhao, M., Pang, L., Liu, M., Yu, S., and Mao, X. “Control Strategy for Helicopter Thermal Management System Based on Liquid Cooling and Vapor Compression Refrigeration.” *Energies*, Vol. 13, No. 9, 2020, p. 2177. https://doi.org/10.3390/en13092177.
[44] Michalak, T., Emo, S., and Ervin, J. “Control Strategy for Aircraft Vapor Compression System Operation.” *International Journal of Refrigeration*, Vol. 48, 2014, pp. 10–18. https://doi.org/10.1016/j.ijrefrig.2014.08.010.
[45] Kellermann, H., Fuhrmann, S., Shamiyeh, M., and Hornung, M. “Design of a Battery Cooling System for Hybrid Electric Aircraft.” *Journal of Propulsion and Power*, Vol. 38, No. 5, 2022, pp. 736–751. https://doi.org/10.2514/1.B38695.
[46] Kang, H., Heo, J., and Kim, Y. “Performance Characteristics of a Vapor Compression Cooling Cycle Adopting a Closed-Loop Air-Circulation System for Avionic Reconnaissance Equipment.” *International Journal of Refrigeration*, Vol. 35, No. 4, 2012, pp. 785–794. https://doi.org/10.1016/j.ijrefrig.2011.11.021.
[47] Saltzman, D., Bichnevicius, M., Lynch, S., Simpson, T. W., Reutzel, E. W., Dickman, C., and Martukanitz, R. “Design and Evaluation of an Additively Manufactured Aircraft Heat Exchanger.” *Applied Thermal Engineering*, Vol. 138, 2018, pp. 254–263. https://doi.org/10.1016/j.applthermaleng.2018.04.032.
[48] Mahmoud, D., Tandel, S. R. S., Yakout, M., Elbestawi, M., Mattiello, F., Paradiso, S., Ching, C., Zaher, M., and Abdelnabi, M. “Enhancement of Heat Exchanger Performance Using Additive Manufacturing of Gyroid Lattice Structures.” *The*

International Journal of Advanced Manufacturing Technology, Vol. 126, Nos. 9–10, 2023, pp. 4021–4036. https://doi.org/10.1007/s00170-023-11362-9.

[49] Da Silva, R. P. P., Mortean, M. V. V., De Paiva, K. V., Beckedorff, L. E., Oliveira, J. L. G., Brandão, F. G., Monteiro, A. S., Carvalho, C. S., Oliveira, H. R., Borges, D. G., and Chastinet, V. L. "Thermal and Hydrodynamic Analysis of a Compact Heat Exchanger Produced by Additive Manufacturing." *Applied Thermal Engineering*, Vol. 193, 2021, p. 116973. https://doi.org/10.1016/j.applthermaleng.2021.116973.

[50] Torri, F., Berni, F., Fontanesi, S., Mantovani, S., Giacalone, M., Defanti, S., Bassoli, E., and Colombini, G. Evaluation of TPMS Structures for the Design of High Performance Heat Exchangers. Presented at the 16th International Conference on Engines & Vehicles, Capri, Italy, 2023.

[51] Careri, F., Khan, R. H. U., Todd, C., and Attallah, M. M. "Additive Manufacturing of Heat Exchangers in Aerospace Applications: A Review." *Applied Thermal Engineering*, Vol. 235, 2023, p. 121387. https://doi.org/10.1016/j.applthermaleng.2023.121387.

[52] Anwajler, B. "Potential of 3D Printing for Heat Exchanger Heat Transfer Optimization—Sustainability Perspective." *Inventions*, Vol. 9, No. 3, 2024, p. 60. https://doi.org/10.3390/inventions9030060.

[53] MIL-PRF-87252E: Performance Specification Coolant Fluid, Hydrolytically Stable, Dielectric. Mar 21, 2018.

[54] Dever, T. P., and Jansen, R. H. Cable Key Performance Parameters for Megawatt Electrified Aircraft Propulsion Conceptual Aircraft Model. Presented at the 2022 IEEE/AIAA Transportation Electrification Conference and Electric Aircraft Technologies Symposium (ITEC+EATS), Anaheim, CA, USA, 2022.

[55] Dever, T., Lantz, T., and Jansen, R. Cable Key Performance Parameter Projections for Megawatt Electrified Aircraft Propulsion Models. Presented at the AIAA SCITECH 2024 Forum, Orlando, FL, 2024.

[56] SAE International. AS210: Definition of Commonly Used Day Types. SAE International, Nov, 2018.

[57] Stalcup, E. J., and Heersema, N. Thermal Requirements for Design and Analysis of Subsonic Single Aft Engine (SUSAN) Research Aircraft. Presented at the AIAA SCITECH 2023 Forum, National Harbor, MD & Online, 2023.

[58] Denham, C. L., Chau, T., Ryan, W., and Jansen, R. Mission Profiles for the SUSAN Electrofan Concept. Presented at the AIAA SCITECH 2023 Forum, National Harbor, MD & Online, 2023.

[59] Sachs-Wetstone, J., Litt, J. S., Kratz, J. L., and Buescher, H. SUbsonic Single Aft eNgine (SUSAN) Power/Propulsion System Control Architecture Updates. Presented at the AIAA SCITECH 2024 Forum, Orlando, FL, 2024.

[60] Chapman, J. W., Lavelle, T. M., May, R. D., Litt, J. S., and Guo, T.-H. *Toolbox for the Modeling and Analysis of Thermodynamic Systems (T-MATS) User's Guide*. Publication NASA/TM-2014-216638. 2014.

[61] Bell, M. E., and Litt, J. S. *Electrical Modeling and Thermal Analysis Toolbox (EMTAT) User's Guide*. Publication NASA/TM-20205008125. 2020.

[62] White, A. S., Waddington, E., Merret, J. M., Greitzer, E. M., Ansell, P. J., and Hall, D. K. System-Level Utilization of Low-Grade, MW-Scale Thermal Loads for Electric Aircraft. Presented at the AIAA AVIATION 2022 Forum, Chicago, IL & Virtual, 2022.

[63] Drela, M. "Aerodynamics of Heat Exchangers for High-Altitude Aircraft." *Journal of Aircraft*, Vol. 33, No. 1, 1996, pp. 176–184. https://doi.org/10.2514/3.46919.

[64] Kellermann, H., Lüdemann, M., Pohl, M., and Hornung, M. "Design and Optimization of Ram Air–Based Thermal Management Systems for Hybrid-Electric Aircraft." *Aerospace*, Vol. 8, No. 1, 2020, p. 3. https://doi.org/10.3390/aerospace8010003.

[65] Meredith, F. W. *Cooling of Aircraft Engines with Special Reference to Ethylene Glycol Radiators Enclosed in Ducts*. Publication 1683. Aeronautical Research Committee, 1935.